Spectroscopic properties of a prototypic organic semiconductor: The case of PTCDA

R. Scholz, I. Vragović, A.Yu. Kobitski, G. Salvan, T.U. Kampen, M. Schreiber, and D.R.T. Zahn

Institut für Physik, Technische Universität, D-09107 Chemnitz, Germany

Summary. — In the present work, we derive a quantitative interpretation for the large Stokes shift observed in crystalline PTCDA (3,4,9,10-perylene tetracarboxylic dianhydride). This issue requires both a microscopic analysis of the isolated molecule and the interactions between the molecules in the crystalline phase. The starting point is the computation of the deformation of the isolated molecule in the relaxed excited state, resulting in elongations of internal vibrational modes. On this basis, we can model the linear absorption of dissolved PTCDA monomers. As the elongations of the internal vibrations can also be observed in resonant Raman spectra obtained on epitaxial films, we conclude that the internal geometric changes in the relaxed excited state are only weakly influenced by the surroundings. However, the optical properties in crystalline films are strongly altered by exciton transfer between neighbouring molecules. From microscopic calculations of the Frenkel exciton transfer, we deduce a consistent set of model parameters for a quantitative interpretation of recent experimental data concerning the linear optical properties of bulk PTCDA. On this basis, we can compute the **k**-space dispersion of the excitonic transitions, resulting in a minimum at the boundary of the Brillouin zone. The origin of the low-temperature photoluminescence can be assigned to this low-lying excited state, while the room-temperature photoluminescence is attributed to charge transfer recombination between positively and negatively charged stack neighbours. First generalizations of the Frenkel exciton transfer model to ultrathin films are discussed.

PACS 78.40.Me – Optical properties, Organic compounds and polymers.
PACS 33.20.Kf – Molecular spectra, Visible spectra.

1. – Introduction

Organic semiconductors have become interesting candidates for various technological applications, ranging from light emitting diodes (LEDs) over solar cells to field effect transistors. Even though organic LEDs and displays are already commercially available, the key properties like electronic transport and linear optical properties in these materials are much less understood than in their inorganic counterparts. *E.g.*, in the case of one of the best studied organic materials, PTCDA, for the dominating absorption band in the visible, the nature of the excitons involved is still open to debate.

PTCDA is a prototypic layered material, where two nearly coplanar molecules in the monoclinic unit cell arrange in the so-called herringbone structure, cf. fig. 1, and consecutive layers grow in inclinated stacks [1]. Previous attempts to model the optical properties of the crystalline phase range from applications of large-radius Wannier-Mott excitons [2] over Frenkel excitons to charge transfer (CT) excitons [3]. Both the epitaxy and the early spectroscopic investigations and model approaches have been summarized in a review paper by S. R. Forrest [4]. As already the monomer spectra show pronounced vibrational bands, all exciton models have to be combined with the elongation of an effective internal mode, as proposed for Wannier-Mott excitons [3, 4], dimer models [5, 6], and one-dimensional stack geometries [7].

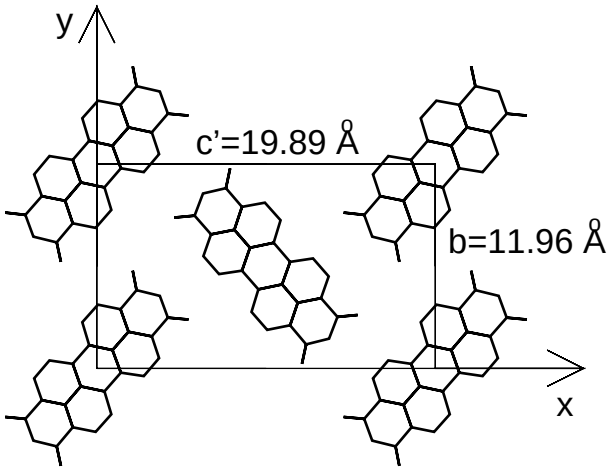

Fig. 1. – Crystal unit cell of α-PTCDA, in the plane most closely coinciding with the molecular planes, where $\mathbf{c}'$ corresponds to the ($\mathbf{c} - 2\ \mathbf{a}$) direction of the published crystal basis vectors [1]. The HOMO-LUMO transition dipoles are oriented along the long axes of the molecules which form an angle of $\varphi = 50.4^0$ with the x-axis.

After presenting the spectroscopic properties of crystalline PTCDA in sect. **2**, we review the displaced harmonic oscillator in sect. **3**. Section **4** is devoted to resonant Raman spectra of PTCDA crystals and epitaxial films, which can be interpreted in terms of the

internal deformation of excited PTCDA molecules. As will be shown in detail, density functional calculations are suitable both for the calculation of the molecular deformation and the vibrational eigenstates [8]. In sect. **5**, we deduce the resulting absorption lineshape and compare with measurements performed on PTCDA dissolved in dimethyl-sulfoxide. Section **6** analyses changes of the optical properties induced by exciton transfer between different molecules in the crystal. Contrary to all previous investigations, we include the full microscopic geometry with two molecules per unit cell, but instead neglect any contributions of CT excitons [9], an approximation which will be motivated later in sect. **8**. Our Frenkel exciton model shows good agreement with existing experimental evidence [10], so that we have a sound basis for an analysis of the **k**-space dispersion occurring for the excitonic transitions. In sect. **7**, the calculated transition energies are compared with the large Stokes shift evidenced in recent photoluminescence (PL) data [11, 12]. In sect. **8**, we discuss time-dependent density functional calculations for monomers and dimers in different geometries. From these calculations, we can exclude any low-lying transition with large oscillator strength which was assumed in recent CT exciton models [7]. Based on dimer calculations performed for molecules in anionic and cationic geometries, we assign the high-temperature PL to CT recombination between positively and negatively charged molecules arranged as stack neighbours. First applications of our Frenkel exciton transfer model to ultrathin films of only a few monolayers are discussed in sect. **9**. The paper is concluded in sect. **10**.

2. – Stokes shift in crystalline PTCDA

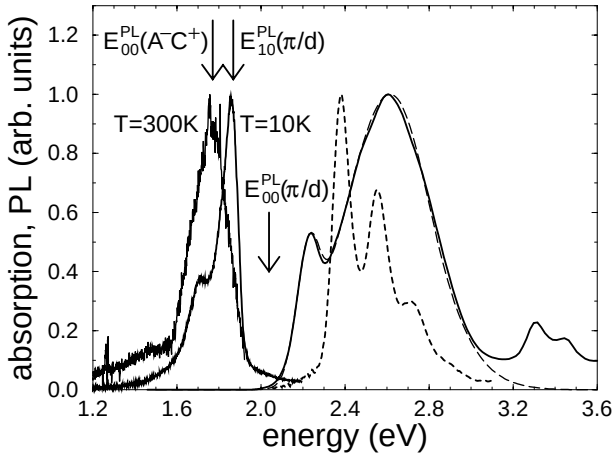

Fig. 2. – Absorption and PL spectra of epitaxial films of PTCDA. Solid lines: experimental absorption coefficient [10], and PL spectra obtained at $T = 10$ K and $T = 300$ K [11, 12]. Long-dashed line: calculated absorption coefficient, cf. sect. **6**. For comparison, the absorption coefficient of PTCDA dissolved in dimethyl-sulfoxide is also shown (short-dashed line) [13]. The assignments of the different PL features are derived in sects. **7** and **8**.

While the absorption and PL spectra of PTCDA dissolved in dimethyl-sulfoxide show the expected mirror symmetry [3, 14], this situation is completely changed in crystalline material or poly-crystalline epitaxial films, cf. fig. 2. Contrary to spectra of PTCDA in solution, no clear vibronic progression can be assigned to the absorption spectra, which instead are considerably broadened. In sect. **6** we will demonstrate that this change in the absorption lineshape can be related to transfer of Frenkel excitons between different molecules. Based on this model calculation, we derive the **k**-space dispersion of the excitonic transitions, resulting in the assignments of the low-temperature PL shown in fig. 2. From time-dependent density functional calculations discussed in sect. **8**, we conclude that at room temperature a second PL mechanism becomes dominating: CT recombination between positively (C^+) and negatively (A^-) charged stack neighbours.

3. – Displaced harmonic oscillator

As a starting point for the subsequent investigations, we review some basic results for the elongation of a single vibrational mode between the geometry in the electronic ground state and the relaxed excited state. Contrary to previous applications of anharmonic potentials to small molecules [15], we will restrict the following discussion to the much simpler harmonic approximation [16].

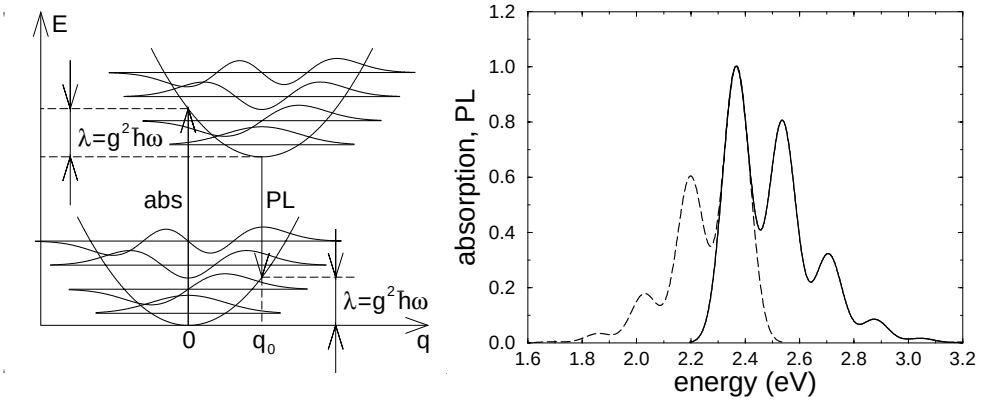

Fig. 3. – Optical cycle including the elongation q_0 of an internal vibration of energy $\hbar\omega$ between the geometry in the electronic ground state and the relaxed excited state. The schematic energy diagram on the left is shown for a vibronic coupling constant $g^2 = 2$, while in the right figure, the absorption (solid line, eqs. (4,5)) and PL (dashed line, eq. (8)) have been calculated for $g^2 = 0.75$, $\hbar\omega = 0.17$ eV, and $E_{00} = 2.365$ eV, corresponding roughly to PTCDA dissolved in dimethyl-sulfoxide. Both spectra are broadened with a Gaussian accounting for the modulation of the HOMO-LUMO transition energy resulting from fluctuations of the solvent environment.

For a dipole-allowed HOMO-LUMO transition and a vibronic energy much larger than the thermal energy, we can assume that the optical absorption starts from the lowest vibronic level in the electronic ground state, $|0_g\rangle$. The transitions to the different

vibronic levels $|\nu_e\rangle$ of the excited state potential have to be weighted with the Franck-Condon factors,

$$S_\nu^2 = |\langle \nu_e | 0_g \rangle|^2 = e^{-g^2} \frac{g^{2\nu}}{\nu!} = P_\nu(g^2), \tag{1}$$

following a Poisson distribution P_ν over the vibronic levels, where the argument g^2 is the vibronic coupling constant. The dielectric function for a given density of molecules N/V can be expressed as

$$\epsilon(\omega) = \epsilon_\mathrm{b}(\omega) + \frac{1}{3} \frac{Ne^2}{V\epsilon_0 m} \sum_{n=0}^{\infty} \frac{f_\mathrm{osc}(\omega_\nu) P_\nu(g^2)}{\omega_\nu} \left[\frac{1}{\omega_\nu - \omega - i\gamma} + \frac{1}{\omega_\nu + \omega + i\gamma} \right] \tag{2}$$

where $\hbar\omega_\nu = E_{0\nu} = E_{00} + \nu\hbar\omega$ is the transition energy $|0_g\rangle \rightarrow |\nu_e\rangle$, m the mass of the electron, and $\epsilon_\mathrm{b}(\omega)$ a frequency-dependent background due to higher-lying transitions. The dimension-less oscillator strength can be related to the electronic transition dipole:

$$f_\mathrm{osc}(\omega_\nu) = |\langle \varphi_\mathrm{LUMO} | \mathbf{r} | \varphi_\mathrm{HOMO} \rangle|^2 \ \frac{2m\omega_\nu}{\hbar}. \tag{3}$$

The prefactor $\frac{1}{3}$ in eq. (2) accounts for the random orientation of the molecular transition dipoles, *e.g.* in solution. For crystalline films, the well-defined arrangement of the molecules results in a more complicated distribution of the coupling strength over the different Cartesian directions, so that the dielectric function becomes an anisotropic tensor, cf. sect. **6**. Assuming an isotropic dielectric function as in eq. (2), the absorption coefficient follows from the imaginary part of the complex refractive index $n(\omega) = [\epsilon(\omega)]^{1/2}$,

$$\alpha(\omega) = 2 \ \frac{\omega}{c} \ \Im[n(\omega)]. \tag{4}$$

For solutions with low concentration, the influence of the dissolved molecules on the real part of the refractive index can be neglected,

$$\Im[n(\omega)] = \frac{\Im[\epsilon_\mathrm{molecule}(\omega)]}{2\Re[n_\mathrm{solvent}(\omega)]}, \tag{5}$$

with the numerator according to eq. (2). Due to the uncertainty principle and thermal motion, the positions and orientations of the solvent molecules fluctuate, resulting in a modulation of the electronic transition energy E_{00} of the dissolved molecules. Usually, these fluctuations are modelled as a temperature-dependent Gaussian broadening of the vibronic progression in eq. (2), cf. also fig. 3.

The lowest moments of the Poisson distribution (1) have a clear physical interpretation: The first moment gives the reorganization energy λ, coinciding with the energies

measured with respect to the classical potential minima in fig. 3, while the second moment can be related to the linewidth of the electronic transition:

$$\begin{aligned} \langle E \rangle &= E_{00} + g^2 \hbar\omega = E_{00} + \lambda \\ \Delta E &= \sqrt{\langle (E - \langle E \rangle)^2 \rangle} = g\hbar\omega \end{aligned} \tag{6}$$

At finite temperature, the vibronic levels of the electronic ground state are populated according to Bose-Einstein statistics. This results in an increase of the broadening with temperature,

$$\Delta E = g\hbar\omega \sqrt{1 + 2n_{\mathrm{th}}(\hbar\omega, k_B T)}, \tag{7}$$

where $n_{\mathrm{th}}(\hbar\omega, k_B T)$ is the number of thermally excited quanta. For low-temperature PL, the rates of recombination to different vibronic sublevels $|\nu_g\rangle$ can be derived from the Einstein coefficient for spontaneous emission [17],

$$\Gamma(|0_e\rangle \to |\nu_g\rangle) = \frac{e^2 |\langle \varphi_{\mathrm{LUMO}} | \mathbf{r} | \varphi_{\mathrm{HOMO}} \rangle|^2 \omega_\nu^3}{3\pi\epsilon_0 \hbar c^3} P_\nu(g^2), \tag{8}$$

with $\hbar\omega_\nu = E_{\nu 0} = E_{00} - \nu\hbar\omega$. In resonant Raman spectra, the vibronic mode yields a cross section proportional to g^2,

$$\sigma_R \propto \; g^2 \; (\hbar\omega)^2 \left[1 + n_{\mathrm{th}}(\hbar\omega, k_B T)\right], \tag{9}$$

where the further prefactors are independent of the elongation of the internal mode to leading order [18, 19]. Therefore, in the case of a large molecule like PTCDA, resonant Raman spectra allow to investigate the elongations of different vibrational modes in the relaxed excited state.

4. – Resonant Raman spectra of epitaxial films

4˙1. *Molecular geometry and orbitals.* – The resonant Raman spectra discussed in this sect. were obtained on 100 nm PTCDA films grown with organic molecular beam deposition (OMBD) on H-passivated Si(111) [20], and their analysis is based on a density functional tight-binding (DFTB) method as discussed elsewhere in more detail [8, 21]. The ground state geometry of the monomer was calculated with the PBE functional [22] in an optimized tight-binding basis. The reliability of our D_{2h} geometry has been tested with the same functional and a larger variational basis as used in the NRLMOL code [23], resulting in an agreement of better than 0.5% r.m.s. variation for the bond lengths between the heavy atoms. For the ground state geometry, the charge densities of the HOMO and LUMO are shown in fig. 4. Our relaxed excited state geometry was found by optimizing the geometry in a conjugate gradient scheme after promoting a HOMO electron to the LUMO, keeping the occupation numbers $n_{\mathrm{HOMO}} = n_{\mathrm{LUMO}} = 1$ fixed.

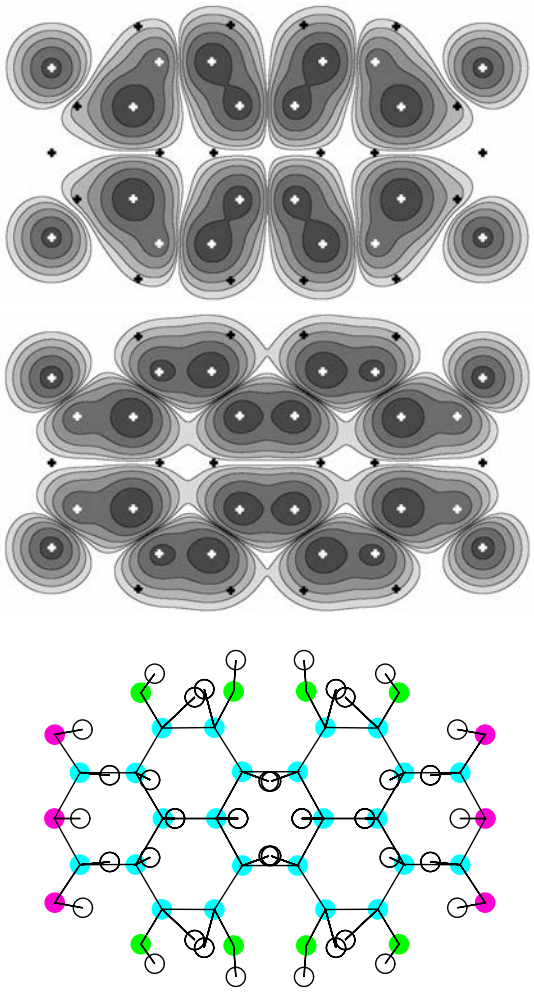

Fig. 4. – Electron density of the $A_u(xyz)$ HOMO (upper panel) and $B_{1g}(yz)$ LUMO (middle) of a PTCDA monomer, as calculated with the DFTB method in the ground state geometry, and deformation between relaxed excited state and ground state geometry (lower panel). In the latter case, the gray circles represent the ground state geometry, and the open circles the deformation in the relaxed excited state (enlarged by a factor of 40). The electron densities of the two orbitals are shown at a distance of 1 Bohr radius above the molecular plane, with the atomic positions indicated by the + symbols. Both the HOMO and the LUMO wavefunctions change sign between consecutive lobes of the electronic density.

The details of the deformation pattern can be understood from the bonding and anti-bonding regions of the two orbitals involved in the optical transition: Bonds become

longer where a bonding region of the HOMO is replaced by a repulsive node of the LUMO, and they shorten in regions where a HOMO node disappears in the LUMO wavefunction.

4˙2. *Resonant Raman spectra of internal vibrational modes.* – The resonant Raman spectra obtained on epitaxial films in back-scattering geometry are displayed in fig. 5. The Raman cross sections of the different modes j can be calculated from the reorganization energies $\lambda_j = g_j^2 \hbar\omega_j$ according to eq. (9), with mode-specific vibrational coupling constants g_j. In the DFTB calculation, the reorganization energy of each mode can be obtained by projecting the total deformation of the molecule on the complete set of vibrational eigenvectors.

As the charge densities of all orbitals transform according to the A_g representation of D_{2h}, the total deformation pattern towards the relaxed excited state conserves the full rectangular symmetry, so that only A_g breathing modes can be elongated. The calculated mode frequencies are indicated below the experimental spectra in fig. 5, with a r.m.s. deviation from the measured positions of 32 cm^{-1} [24, 25]. The calculated Raman cross sections are in reasonable agreement with the measured ones, cf. Ref. [8] for a more detailed discussion.

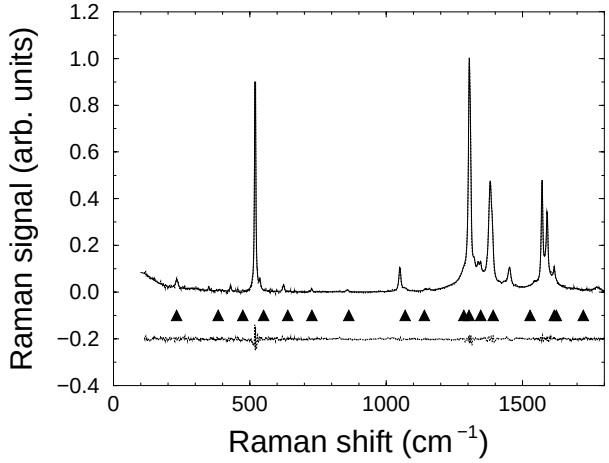

Fig. 5. – Resonant Raman spectra of PTCDA epitaxial films grown on H-passivated Si at room temperature, obtained at a laser energy $E_L = 2.54$ eV (Ar^+ laser line $\lambda = 488$ nm). As the experimental spectra (dots) and the multi-Lorentzian fit (solid line) are nearly indistinguishable on the scale shown, we also report the residuals of the fits (dots, shifted for clarity). The peak at 520 cm^{-1} is the optical phonon of the substrate, and the calculated A_g modes are indicated as triangles.

4˙3. *Resonant Raman spectra of external phonon modes.* – Epitaxial films obtained with OMBD at room temperature are dominated by α-PTCDA, crystallizing in the monoclinic space group $C_{2h}(2/m)$ $(P2_1/c)$ with two molecules per unit cell. This results

in 12 phonon branches: three acoustic translational, three optic translational and six optic rotational phonons (librational phonons). The translational optic phonons are infrared active only, whereas the librational modes with even parity are Raman active. Even though their frequencies are quite low, they result in considerable Raman cross sections because their vibrational coupling constants g_j^2 are large, cf. fig. 6 [29, 30, 31].

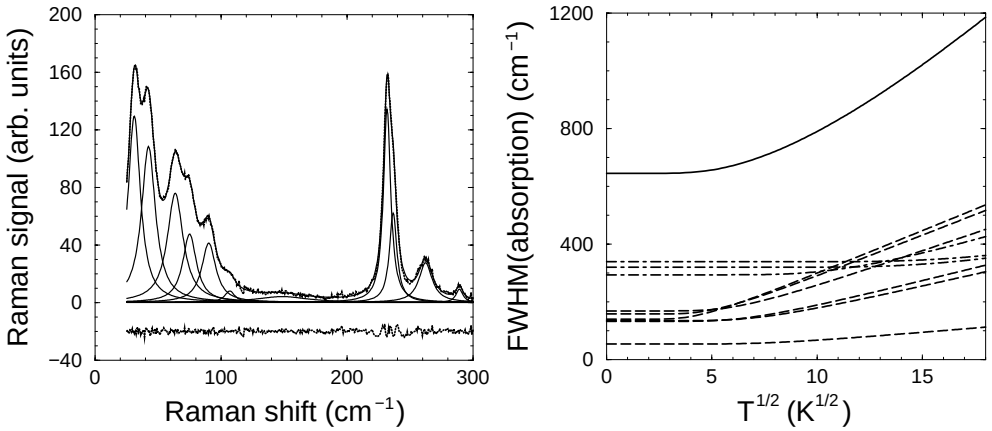

Fig. 6. – Left: Resonant Raman spectra obtained at $E_L = 2.54$ eV on a PTCDA film grown by OMBD on S-passivated GaAs(100). Both the experimental spectra and the fit residuum (shifted for clarity) are shown as dots. The external phonon modes appear below 120 cm^{-1}, and the lowest internal mode (around 232 cm^{-1}) shows a small Davydov splitting. Features above 250 cm^{-1} are related to the substrate optical phonon and the lower plasmon-phonon coupled mode. The different contributions to the multi-Lorentzian fitting functions are displayed separately (solid lines). Right: Temperature dependence of the contributions to the absorption linewidth according to eq. (7), with external modes (dashed lines), the three lowest internal A_g modes (dash-dotted lines), and total (solid line).

From the multi-Lorentzian fit in fig. 6 and eq. (9), we can deduce the vibrational coupling constants g_j^2 for each mode, normalized to the calculated value $g_1^2 = 0.287$ for the lowest internal mode $\hbar\omega_1 = 232$ cm^{-1} [8]. Together with eq. (7), this allows an estimate of the contributions to the linewidth in linear absorption. At room temperature, the resulting full width half maximum (FWHM) is about 1150 cm^{-1} or 0.14 eV. Gaussian broadenings of similar magnitude will be discussed again with respect to the calculations of linear absorption in crystalline PTCDA in sect. **6**, and they are the reason why the thin film absorption displayed in fig. 2 does not show a clear vibronic substructure.

5. – Monomer absorption

From the calculated reorganization energy λ_j of each internal mode, we can derive the vibronic coupling constant g_j^2 occurring in the corresponding Poisson progression, cf. eq. (1). For the absorption of the molecule, the vibronic progressions of all 19 internal A_g modes have to be multiplied, cf. fig. 7. The first observed sideband is

obviously composed of several A_g modes, but due to additional broadening effects this sub-structure cannot be resolved. For the higher harmonics, the number of contributing sum frequencies rises, resulting in an apparent increase of the linewidth. After a suitable Gaussian broadening of FWHM = 850 cm^{-1}, the different discrete levels merge into large bands, with the first harmonics corresponding to a Poisson progression with an *effective* argument of 1.18 (summed over the A_g modes involved), somewhat higher than in the observed spectrum.

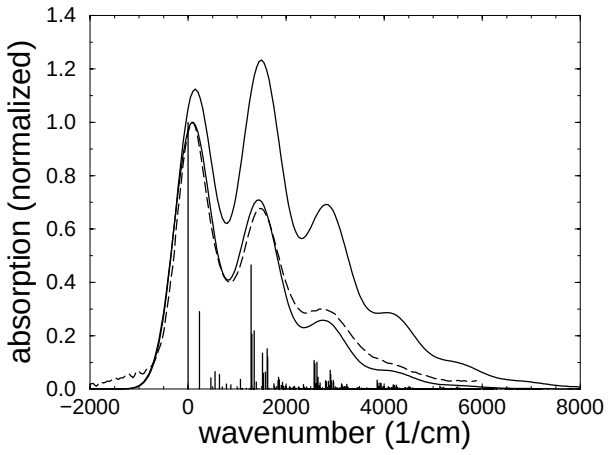

Fig. 7. – Linear absorption of PTCDA dissolved in dimethyl-sulfoxide. Dashed: experimental spectra [13], discrete vertical lines: multi-Poisson distribution of elongated A_g modes, solid lines: absorption spectra derived from the discrete transitions and a Gaussian broadening of 850 cm^{-1}. For the lower solid curve, the calculated reorganization energies have been reduced by a factor of 0.65. In this figure, we use E_{00} as the reference energy, *i.e.* the experimental curve is shifted by 2.365 eV (19075 cm^{-1}). The experimental absorption spectra are similar to earlier investigations [3] and PL excitation spectra [14].

In order to achieve a better agreement with the experimental spectra, we assume a reduction of the reorganization energies λ_j and the corresponding arguments of the Poisson progressions g_j^2 by a factor of 0.65. Such a reduction can be motivated by screening effects induced by the high dielectric constant of the solvent [32], which are beyond our density functional calculation of an isolated molecule. For PTCDA molecules isolated in a quartz glass matrix, the infrared dielectric constant of the glass is close to unity in the region of about 1400 cm^{-1} where the most prominent Raman modes occur. In this case, we do not expect any dielectric screening induced by the matrix material, and indeed it can be shown that the calculated elongations are quite realistic [33].

The agreement between our DFTB approach and the measured monomer spectra is similar to earlier model calculations [34]. From the good overall correspondence of both the calculated absorption and the resonant Raman spectra with the experimental findings, we conclude that the internal deformation of the excited molecules in the epitaxial

film is mainly determined by the node patterns of the monomer orbitals, as displayed in fig. 4.

6. – Exciton transfer

6˙1. *Model Hamiltonian.* – As in previous investigations of excitonic effects in crystalline PTCDA, we assume in the following that the internal deformation of the relaxed excited molecules can be summarized by an *effective* vibrational mode of about $\hbar\omega = 0.17$ eV and a corresponding vibrational coupling constant g. Based on Pauli operators for creation ($b^+_{i\alpha\nu}$) and annihilation ($b_{i\alpha\nu}$) of a Frenkel exciton (in molecule α at crystal site $\mathbf{R}_i$ in vibrational sublevel ν), we start with a model Hamiltonian in Heitler-London approximation allowing for exciton transfer [35, 36],

$$H = \sum_{i\alpha\nu} E_{0\nu} b^+_{i\alpha\nu} b_{i\alpha\nu} + \sum_{i\alpha\nu} \sum_{j\beta\mu} t_{i\alpha\nu;j\beta\mu} b^+_{i\alpha\nu} b_{j\beta\mu} \ , \tag{10}$$

where $E_{0\nu} = E_{00} + \nu\hbar\omega$ is the exciton on-site energy of the exciton in the νth vibrational level, composed of the transition energy E_{00} between the vibrational ground states, and a vibronic part. The reference energy E_{00} we use in the following already contains environment-dependent shifts, *i.e.*, it does not necessarily coincide with the reference energy $E_{00} = 2.365$ eV for monomers dissolved in dimethyl-sulfoxide, *cf.* fig. 7.

After a decomposition of the transfer matrix element $t_{i\alpha\nu;j\beta\mu}$ into an electronic and a vibronic part,

$$t_{i\alpha\nu;j\beta\mu} = T_{i\alpha;j\beta} S_\nu S_\mu, \tag{11}$$

and a Fourier transformation of the Hamiltonian (10) to $\mathbf{k}$-space, we obtain the following block Hamiltonian for each wave vector:

$$H(\mathbf{k}) = \begin{pmatrix} H_{AA}(\mathbf{k}) & H_{BA}(\mathbf{k}) \\ H_{AB}(\mathbf{k}) & H_{BB}(\mathbf{k}) \end{pmatrix} \tag{12}$$

where *e.g.* the block $H_{AA}(\mathbf{k})$ stands for the interaction of the basis molecule A with the A molecules in the other unit cells. The blocks have the following structure concerning the vibrational levels μ, ν:

$$\begin{aligned} H_{AA;\mu\nu}(\mathbf{k}) &= H_{BB;\mu\nu}(\mathbf{k}) \\ &= E_{0\nu}\delta_{\mu\nu} + S_\mu S_\nu \sum_{j\neq 0} e^{i\mathbf{k}\cdot\mathbf{R}_j} T_{0A;jA} \end{aligned} \tag{13}$$

$$H_{AB;\mu\nu}(\mathbf{k}) = H^*_{BA;\nu\mu}(\mathbf{k}) = S_\mu S_\nu \sum_j e^{i\mathbf{k}\cdot\mathbf{R}_j} T_{0A;jB} \tag{14}$$

The sum over the transfer between equivalent molecules in eq. (13) will be abbreviated by $X(\mathbf{k})$ in the following, the sum in eq. (14) by $V(\mathbf{k})$. As both basis molecules are

included in the Hamiltonian in the same way, all resulting eigenstates possess even or odd symmetry with respect to exchange of A and B molecules. It can be shown analytically that the Hamiltonian decouples into the two corresponding subblocks, with a vibronic structure like eq. (13), but transfer matrix elements $X+V$ and $X-V$, respectively.

6˙2. *Linear optical properties.* – Due to the small wave vector of the photon, a calculation of the linear optical properties requires to take into account only the immediate surroundings of the Γ-point of the Brillouin zone. In the following, we make the assumption that the crystallites in the epitaxial film have a finite size, so that the non-analyticity problems arising at $\mathbf{k}=0$ for an infinite crystal discussed earlier [35] disappear. All distance-dependent interactions between different molecular sites are calculated from the distributions of the transition dipoles over the molecular sheets, and the anisotropic static dielectric tensor of α-PTCDA [37, 38]. As discussed earlier for cubic systems, the dielectric screening develops on a spatial scale corresponding roughly to the bond length [39], so that for the anisotropic system studied here, we expect that the Coulomb interaction between the transition dipoles of two molecules is always fully screened, with the exception of the stack neighbours. Therefore, we found it convenient to divide the interaction X between the same basis molecules into the parts W arising from the stack neighbours, and the remaining part M of the sum which can be calculated with the bulk value of the dielectric tensor, $X(\mathbf{0}) = \sum_{j\neq 0} T_{0A;jA} = 2W(\mathbf{0}) + M(\mathbf{0})$, where $M(\mathbf{0}) = \sum'_{j\neq 0} T_{0A;jA}$ excludes the stack neighbours. We evaluate this sum and the corresponding expression $V(\mathbf{0}) = \sum_j T_{0A;jB}$ inside a sphere in terms of lattice parameters, corresponding to ellipsoids in real space. For a radius of 35 lattice parameters containing somewhat more than 10^5 unit cells, we found that the sums show only a weak dependence on the crystallite radius: For a transition dipole of $d = 6.45$ Debye, the exciton transfer energies are $M(\mathbf{0}) = -0.014$ eV and $V(\mathbf{0}) = 0.034$ eV [9].

In order to compare our model with the experimental results [10], we diagonalize the model Hamiltonian with a consistent parameter set, resulting in best fit values of $X(\mathbf{0}) = 0.150$ eV and $V(\mathbf{0}) = 0.047$ eV, where the latter value agrees reasonably well with the microscopic calculation. The results are displayed in fig. 8. As the measured data are not fully Kramers-Kronig consistent and contain a tail in the exctinction coefficient beyond 3.0 eV where no electronic transitions are expected except for the pair around 3.4 eV, we fit the extinction coefficient after elimination of this tail. From the fitted value for X and the microscopic calculation for M, we deduce an interaction between stack neighbours of $W = W(\mathbf{0}) = \frac{1}{2}[X(\mathbf{0}) - M(\mathbf{0})] = 0.082$ eV, between the values obtained from microscopic calculations for the two limiting cases including full screening with the bulk dielectric tensor, $W = 0.021$ eV, and the unscreened ($\epsilon = 1$) interaction, $W = 0.094$ eV. Actually, a somewhat lower value of V like the one found in our microscopic calculation gives similar results for $\epsilon_{||} = \frac{1}{2}(\epsilon_{xx} + \epsilon_{yy})$ and the resulting refractive index, except that the reduction of the tail in the extinction coefficient develops already at slightly lower energies. The broadening of FWHM = 123 meV used for the lowest vibronic level is about 20 meV below the linewidth assigned to the external Raman-active modes and the lowest internal A_g modes, cf. fig. 6. As this somewhat larger linewidth was normalized to the calculated

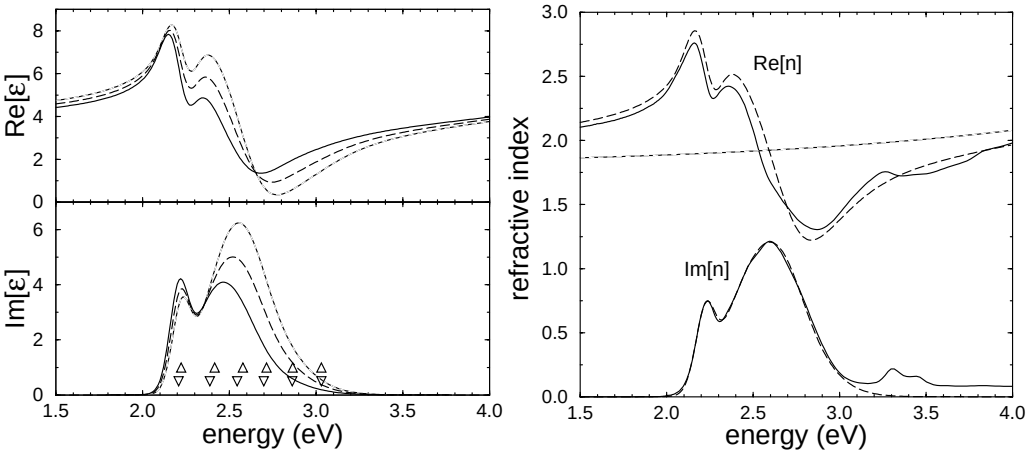

Fig. 8. – Left: Diagonal components of the frequency-dependent dielectric tensor, assuming the same background for both directions, ϵ_{xx} (solid lines), ϵ_{yy} (dotted lines), average (dashed lines). The different vibronic levels for the upper Davydov component ($\triangle$, contribute to ϵ_{yy}) and lower Davydov component ($\triangledown$, contribute to ϵ_{xx}) are also shown. Right: Real and imaginary part of the refractive index of PTCDA films, based on the average dielectric function $\epsilon_{||} = \frac{1}{2}(\epsilon_{xx} + \epsilon_{yy})$. Solid lines: experimental data obtained on poly-crystalline PTCDA films grown on quartz glass [10], dashed lines: present model calculation, and background (dotted line) for the real part of the refractive index, modelled as a higher lying transition at 7.5 eV. Further parameters: $E_{00} = 2.18$ eV, $\hbar\omega = 0.17$ eV, $g^2 = 1.0$, $X(\mathbf{0}) = 0.150$ eV, $V(\mathbf{0}) = 0.047$ eV, broadening of the vibronic levels: $\mathrm{FWHM}_0 = 0.123$ eV, increasing for the higher harmonics to $\mathrm{FWHM}_1 = 0.283$ eV, $\mathrm{FWHM}_2 = 0.293$ eV, $\mathrm{FWHM}_3 = 0.400$ and $\mathrm{FWHM}_4 = \mathrm{FWHM}_5 = 0.433$ eV [9].

elongation of the lowest internal A_g mode, this is a further indication that the calculated internal deformations in the relaxed excited state of the monomer are slightly larger than for molecules in the crystalline phase. The larger broadenings needed for the higher harmonics result from interactions between the different A_g modes contributing, compare fig. 7. Therefore, in a multi-mode model of exciton transfer, we expect that a unique Gaussian broadening for the whole spectra would be sufficient.

In the above comparison with the experimental data [10], the anisotropy of our calculated dielectric function was averaged out because the crystallites in the films have a random azimuthal orientation, but with the planes displayed in fig. 1 parallel to the substrate surface [10]. Even though the Davydov splitting between the two diagonal elements is quite small, cf. fig. 8, the corresponding oscillator strengths result in a pronounced difference between the lineshapes. Qualitatively similar anisotropies of the dielectric tensor were observed in recent ellipsometric investigations of PTCDA crystals [40], the main difference being a larger estimate for the transition dipole.

6˙3. *k-space dispersion of excitonic transitions.* – After a microscopic estimate of the quantities $X(\mathbf{k})$ and $V(\mathbf{k})$, we can diagonalize the Hamiltonian (12) for any wave vector. As a reference value, we take again $W(\mathbf{0}) = 0.082$ eV, and calculate both $M(\mathbf{k})$ and $V(\mathbf{k})$

microscopically. The largest dispersion develops along the direction orthogonal to the plane shown in fig. 1. It is dominated by the interactions among stack neighbours, so that the interaction parameter at the boundary of the Brillouin zone is close to $-2W(\mathbf{0})$: $X(\mathbf{k}=(0,0,\frac{\pi}{d}))=-0.158$ eV, where $d=3.2$ Å is the stacking distance.

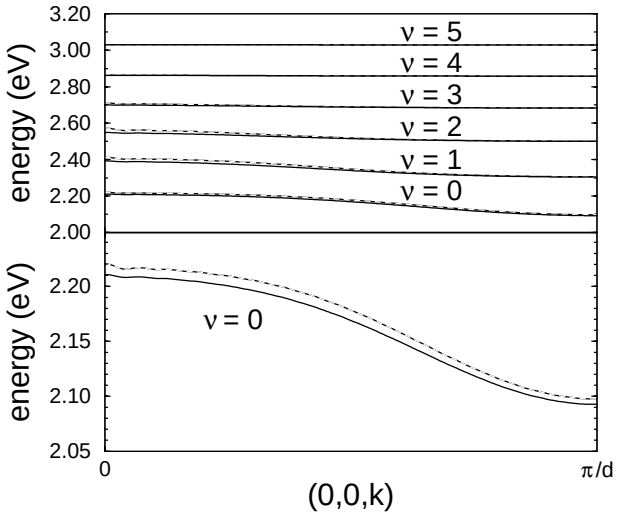

Fig. 9. – Dispersion of the excitonic transitions $E_{0\nu}$ for wave vectors orthogonal to the plane shown in fig. 1. The inter-layer distance along this direction is $d=3.2$ Å. Upper: dispersion of vibrational sublevels $E_{0\nu}$ for $\nu=0,..,5$, lower: dispersion of the lowest vibrational level $E_{00}(0,0,k)$ on an enlarged scale. Solid lines: calculated from the subblock of the Hamiltonian with $X(\mathbf{k})-V(\mathbf{k})$ contributing to ϵ_{xx} at Γ, dotted lines: calculated from the subblock with $X(\mathbf{k})+V(\mathbf{k})$ resulting in ϵ_{yy} at Γ.

The dispersion along this direction of strongest modulation is shown in fig. 9, while the variation along directions orthogonal to it is nearly one order of magnitude smaller (not shown) [41]. Compared to the transition energy $E_{00}=2.18$ eV entering our model calculation, one can distinguish two main contributions to the lowest vibrational sublevel. First, the energy $E_{00}(0,0,k)$ is shifted by the diagonal elements of the block-diagonalized Hamiltonian, $S_0^2(X(0,0,k)\pm V(0,0,k))$, resulting in a shift upwards at Γ and downwards at the edge of the Brillouin zone by approximately $2S_0^2W(0)\cos(kd)$. Second, the lowest vibronic level is pushed downwards by the interactions with the higher ones, resulting in a shift of $-\sum_{\nu=1}^{5}(S_0S_\nu(X(0,0,k)\pm V(0,0,k))^2/(E_{0\nu}-E_{00})$ in second order perturbation theory, so that the dominating contribution of the stack neighbours is proportional to $-\cos^2(kd)$. A similar dispersion as $E_{00}(0,0,k)$ in fig. 9 has been observed recently for the wave-vector–dependent dielectric function derived from electron energy loss spectroscopy (EELS) on single crystals of α-PTCDA [42].

7. – k-space dispersion and low-temperature photoluminescence

From the **k**-space dispersion shown in fig. 9, it is obvious that the lowest transition at the edge of the Brillouin zone, $E_{00}(0,0,\frac{\pi}{d})$, is far below the value of E_{00} entering our model calculation, which we have fitted to be 2.18 eV, cf. the caption of fig. 8. Taking the lower value of the Davydov doublet, this point of the Brillouin zone shows a transition energy of 2.093 eV. However, this **k**-space dispersion includes only the *effective* internal mode, *i.e.* an average over the dominating Raman modes between 1050 and 1600 cm^{-1} in fig. 5, and the resulting vibronic progression as observed for the monomer absorption in fig. 7. Therefore, we have to assess again the internal vibrational modes far below the effective mode energy of $\hbar\omega = 0.17$ eV. In fig. 7, it is obvious that the elongation of the lowest internal breathing modes results in a deformation of the E_{00} band of the effective mode, shifting its maximum by about 17 meV in the unscaled calculation. Furthermore, external phonon modes below 120 cm^{-1} contribute considerably to the resonant Raman spectra, as evidenced in fig. 6 [29, 30, 31]. Therefore, we divide the reorganization energy λ into the corresponding parts,

$$\lambda_{\mathrm{total}} = \lambda_{\mathrm{ext}} + \lambda_{\mathrm{low}} + \lambda_{\mathrm{high}}. \tag{15}$$

The contribution $\lambda_{\mathrm{high}} = 0.17$ eV has been considered by introducing the effective vibronic mode and was already fully accounted for in our calculation of the **k**-space dispersion. Applying the same scaling of 0.85 as for the effective internal mode ($g^2 = 1.18$ resulting from the monomer calculation $\rightarrow g^2 = 1.0$ in the modelling of exciton transfer) to the other two contributions, we find $\lambda_{\mathrm{low}} = 0.014$ eV for the low frequency internal modes, and $\lambda_{\mathrm{ext}} = 0.041$ eV from the analysis of the resonant Raman cross sections of the external modes, cf. fig. 6. After correcting the excitonic transition energy E_{00} at the edge of the Brillouin zone by these two contributions to the reorganization energy, we find an estimate for the transition energies between the lowest vibronic levels of *all* internal and external vibrations,

$$E_{00}^{\mathrm{PL}}\left(0,0,\frac{\pi}{d}\right) = E_{00}\left(0,0,\frac{\pi}{d}\right) - \lambda_{\mathrm{ext}} - \lambda_{\mathrm{low}} = 2.038 \text{ eV}, \tag{16}$$

which, therefore, is the highest PL transition expected at low temperature. This energy is in reasonable agreement with the upper edge of the high-energy satellite in the PL spectra, compare fig. 2. However, we have to keep in mind that the excitonic transition at $\mathbf{k} = (0,0,\frac{\pi}{d})$ is *indirect* and cannot couple directly to a photon with $\mathbf{k} \approx 0$, so that any PL emission process from this minimum of the exciton dispersion requires the emission or absorption of a vibronic excitation in order to allow for momentum conservation. Therefore, we assign the small high-energy structure observed around 2.0 eV to absorption or emission of very low-lying vibrational modes, *e.g.* external phonons or low-energy internal vibrations. From the weakness of the corresponding PL feature, we conclude that these low-energy phonon scattering processes are rather unlikely.

The maximum of the PL spectra at low temperature can then be assigned to emission of phonons matching approximately our effective mode energy,

$$E_{10}^{\mathrm{PL}}\left(0,0,\frac{\pi}{d}\right) = E_{00}^{\mathrm{PL}}\left(0,0,\frac{\pi}{d}\right) - \hbar\omega = 1.868 \text{ eV}, \tag{17}$$

which is in good agreement with the observed maximum at 1.86 eV. Within this assignment, the final state after emission would be the first vibrational level of the effective mode in the electronic ground state potential. For the efficiency, we expect the same Franck-Condon factors occuring also in absorption into the first vibrational band, $|\langle 1_g|0_e\rangle|^2 = |\langle 1_e|0_g\rangle|^2$, so that it is not surprising that the modes contributing to the first vibrational sideband in fig. 7 are also required for the assignment of the low-temperature PL maximum.

As a scenario for the relaxation of the optical excitation at low temperature, we propose the following. First, a photon is absorbed, creating a Frenkel exciton close to the Γ point. Then, the relaxation towards the edge of the Brillouin zone can be achieved by a vibronic excitation of suitable energy and wave vector, which we suppose to be relatively fast as the lifetime of the corresponding high-frequency vibrational modes should be of the order of picoseconds. This estimate for the lifetime can be deduced both from the linewidth observed in resonant Raman spectra [8] and dephasing times observed in pump-probe spectra on a similar thin film material (Me-PTCDI), where the A_g modes appeared as damped oscillations in real time [43]. The thermalization of the lowest internal vibrations and the external phonons should be somewhat slower because they are excited to rather high vibrational levels and, as a tendency, show longer dephasing times [43] and therefore longer lifetimes. Nevertheless, this thermalization scenario should be accomplished after a few tens of picoseconds, *i.e.* within the resolution of recent time-resolved PL measurements [12]. At later times (some ns), the PL spectra are dominated by a broad structure at lower energy, which could correspond to a CT recombination at room temperature, compare the discussion in the next Section. The longer lifetime of this radiative recombination is in keeping with the smaller oscillator strength obtained in our microscopic calculations for the dimer.

8. – Time-dependent density functional calculations for dimers

8˙1. *Dimer calculations.* – The calculations in the present sect. are based on the experimental geometry of the molecules in α-PTCDA as determined by X-ray scattering [1, 4], and an optimization of the C-H bond geometries using the B3LYP functional in the 3-21G basis set as implemented in the GAUSSIAN98 software [26, 27]. We investigate two different geometries: The stack dimer in the so-defined crystal geometry, and a dimer where the molecular geometries are modified in order to favour low-lying excited states with charge separation. For the latter case, we optimize the neutral molecule and its cation and anion in the rectangular D_{2h} symmetry, record the deformation patterns of the charged molecules, and add them to the experimental stack geometry. With this procedure, we define a dimer without inversion symmetry but with geometries optimized

for a positively and a negatively charged molecule, as discussed elsewhere in more detail [44].

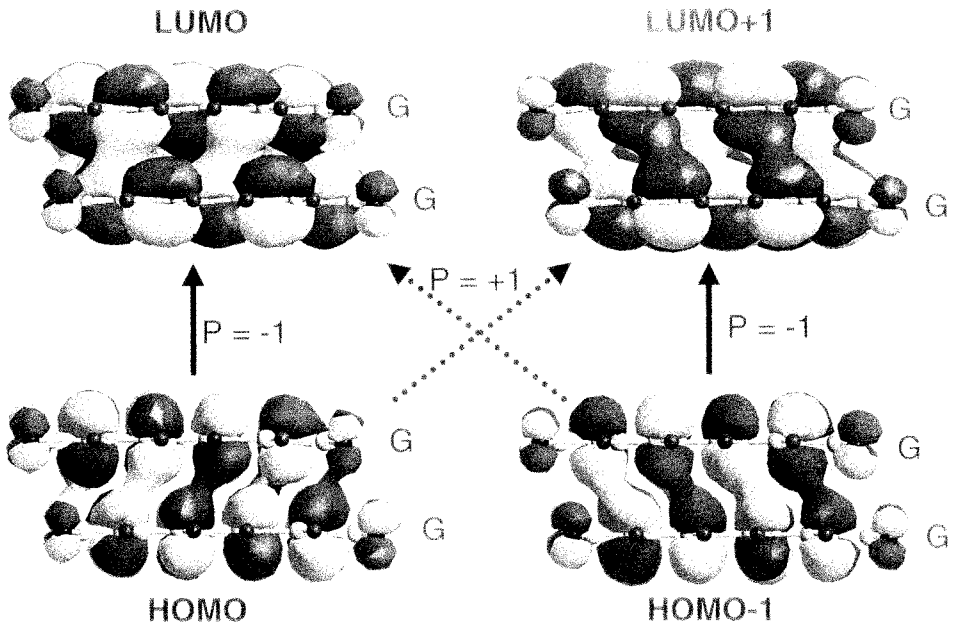

Fig. 10. – Electronic orbitals for the stack dimer in the experimental geometry [1]. The dipole-allowed transitions between the Kohn-Sham orbitals are indicated with solid arrows, the dipole-forbidden transitions with dashed arrows. Regions with positive wavefunction are depicted in light grey, regions with negative wavefunctions in black.

Already the Kohn-Sham orbitals show pronounced differences between the regular stack in fig. 10 and the deformed stack in fig. 11 . In the first case, all single particle orbitals have inversion symmetry with respect to the center of mass of the dimer, *i.e.* they are fully delocalized over both molecules. Therefore, the optical transitions indicated have a well-defined parity, and dipole-allowed transitions ($P = -1$) are easily distinguished from dipole-forbidden transitions ($P = +1$). Using time-dependent density functional theory (TD-DFT), it turns out that the dipole-allowed transitions between the single particle orbitals as depicted in fig. 10 interfere constructively or destructively, resulting in transition energies of 2.73 eV (oscillator strength $f_{\mathrm{osc}} = 0.93$) and 2.19 eV ($f_{\mathrm{osc}} = 0.02$). The dipole-forbidden transitions occur at 2.16 eV and 2.43 eV, with vanishing oscillator strength.

As the TD-DFT calculation is done in Born-Oppenheimer approximation in a frozen geometry, the resulting eigenvalues can be analysed without any coupling to an internal vibrational mode. In the basis of transitions between the localized HOMO and LUMO states of the two molecules in the stack, a suitable Hamiltonian for the resulting transition

energies is simply

$$H = \begin{pmatrix} E_F & W & D_e & D_h \\ W & E_F & D_h & D_e \\ D_e & D_h & E_{CT} & 0 \\ D_h & D_e & 0 & E_{CT} \end{pmatrix}, \tag{18}$$

where E_F is the energy of the Frenkel exciton transition on each of the molecules, E_{CT} the energy for the charge transfer transitions, *e.g.* $\varphi^{(1)}_{\mathrm{HOMO}} \rightarrow \varphi^{(2)}_{\mathrm{LUMO}}$, D_e the electron transfer element between the LUMO states of both molecules, and D_h the hole transfer between the two HOMO states [45]. The transfer of Frenkel excitons is included as W, while the transfer of CT excitons can be neglected as it would involve both an electron and a hole transfer, resulting in a much smaller matrix element than all the other parameters in eq. (18). A basis change to the parity-adapted orbitals as displayed in fig. 10 and the corresponding transitions leads to a decoupling into two subblocks:

$$H^{(P=-1)} = \begin{pmatrix} E_F + W & D_e + D_h \\ D_e + D_h & E_{CT} \end{pmatrix} \tag{19}$$

for the dipole-allowed and

$$H^{(P=+1)} = \begin{pmatrix} E_F - W & D_e - D_h \\ D_e - D_h & E_{CT} \end{pmatrix} \tag{20}$$

for the dipole-forbidden transitions, respectively. From the numerical solutions and the two parity-adapted subblocks, we can easily assign the most important parameters: $E_F = 2.565$ eV for the Frenkel exciton transition energy, $E_{CT} = 2.19$ eV for the CT exciton, and $W = 0.165$ eV for the Frenkel exciton transfer. Except for a small admixture of the Frenkel exciton, the lower parity-allowed transition at 2.19 eV with $f_{\mathrm{osc}} = 0.02$ gives a direct measure of the small oscillator strength of the CT exciton, allowing an *a posteriori* justification of the neglect of the CT transitions in sect. **6**. At the time being, we have no physical interpretation for the large difference between the exciton transfer $W = 0.165$ eV derived from the TD-DFT calculations and the much lower value $W = 0.082$ eV found from the analysis in sect. **6**.

In the case of the deformed stack in fig. 11, the electronic orbitals have no longer a well-defined parity, and we find both delocalized single particle orbitals, *e.g.* for the two highest occupied orbitals, and fully localized orbitals, as for the two lowest unoccupied orbitals. In the latter case, the deformation of the stack results in a considerable splitting of 0.21 eV between the LUMO orbitals in the two molecules. The TD-DFT calculation allows us to distinguish two different types of transitions. Two of the transitions occur again between mainly delocalized orbitals, corresponding to the dipole-allowed transitions in the regular stack, with energies of 2.59 eV ($f_{\mathrm{osc}} = 0.86$) and 2.24 eV ($f_{\mathrm{osc}} = 0.05$), and it can be shown that the oscillator strength of the latter results from the parity violation in the deformed stack. The unoccupied orbitals involved in these transitions are coherent

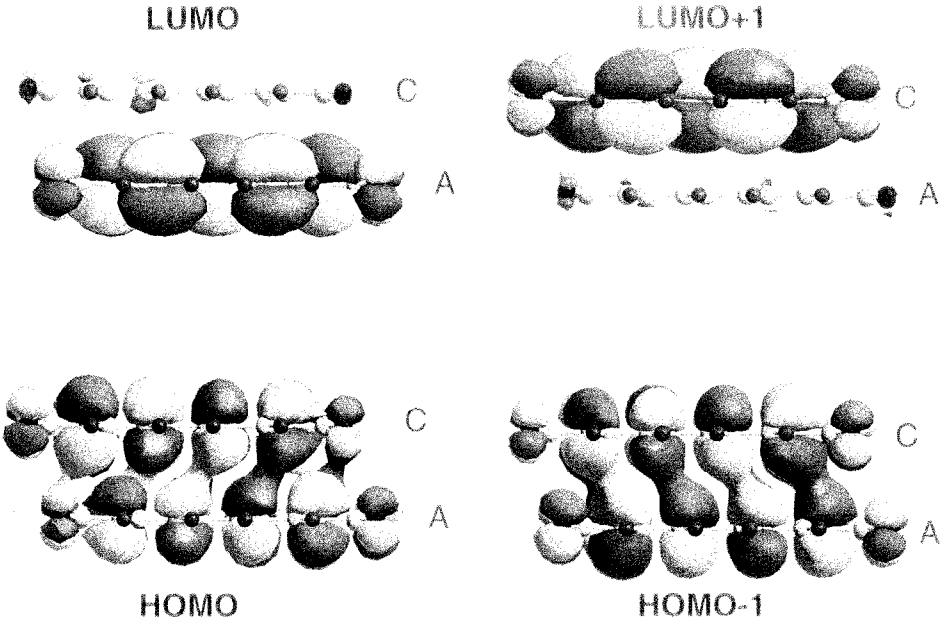

Fig. 11. – Electronic orbitals for the deformed dimer, where the lower molecule has been optimized with an additional negative charge (anionic geometry), the upper with a positive charge (cationic geometry).

superpositions of the LUMO and LUMO+1 orbitals, *i.e.* they resemble the delocalized orbitals in the regular stack as depicted in fig. 10. On the other hand, the calculation gives two transitions between localized states, resulting in charge transfer between both molecules. The more interesting of the two can be interpreted as a transition between the localized HOMO on the cation (*i.e.* a coherent superposition of the highest valence orbitals shown, with constructive interference on the cationic site), and the LUMO on the anionic site. It occurs at 1.86 eV with a very small oscillator strength of $f_{\mathrm{osc}} = 0.01$. Concerning PL, such a transition can be interpreted as CT recombination between two charged stack neighbours, where the excess electron of the anion transfers to the half-filled HOMO on the cationic site. The second transition between localized states would occur at 2.07 eV ($f_{\mathrm{osc}} = 0.01$) and involves the LUMO of the cation and the HOMO of the anion. In PL, this transition does never occur, as the geometry does not favour such a relaxed excited state: It would correspond to a recombination starting from the higher-lying LUMO+1.

8˙2. *Calibration of energy axis.* – In order to eliminate systematic deviations of the TD-DFT energies, we have to relate all energies to the parameters obtained in the calculation of the bulk dielectric function in sect. **6**. In the model of Frenkel exciton transfer, we have used an energy reference of $E_{00} = 2.18$ eV for the monomer, resulting in an average

of $\langle E_{\rm abs}\rangle = E_{00} + g^2\hbar\omega = 2.35$ eV, cf. the parameters in the caption of fig. 8. This has to be compared with the TD-DFT transition energies in the regular dimer with $E_F = 2.565$ eV, or 0.215 eV higher. Such a systematic deviation can be related to deficiencies of the density functional used, to the smallness of the basis set, and to the dimer geometry, where each molecule has only one neighbouring molecule instead of two in the infinite stack. Shifting all the calculated energies by -0.215 eV, we find an estimate for the anion-cation CT recombination of $\langle E_{\rm PL}\rangle = 1.86$ eV $- 0.215$ eV $= 1.645$ eV. However, this is not yet the highest PL feature observable, but an average PL energy, $\langle E_{\rm PL}\rangle = E_{00} - g^2\hbar\omega$. With a reorganization energy of about $\lambda = g^2\hbar\omega = 0.125$ eV which can be estimated from the deformation patterns of the anion and cation geometries and a scaling of 0.85 as for the relaxed excited state, we arrive at an estimate of $E_{00}(\mathrm{A^-C^+}) = 1.645$ eV $+ \lambda = 1.77$ eV, in excellent agreement with the PL band dominating at room temperature, cf. the assignment in fig. 2.

After optical absorption, this type of PL requires a dissociation of the Frenkel exciton into two mobile charges, which subsequently diffuse through the crystal. Eventually, they can be trapped in the energetically most favourable dimer configuration, from where they recombine in a CT PL process. As the relative contribution of the corresponding PL band becomes dominant at room temperature, we expect a small energetic barrier hindering exciton dissociation at low temperature. However, at the time being, details of the corresponding configuration coordinate diagram for charge separation are not yet available. Possibly, the high-temperature PL in PTCDA can be related to self-trapped excitons in similar materials, as discussed, *e.g.*, for the cases of α- and β-perylene [46].

The low-lying dipole-forbidden transitions in the regular dimer in fig. 10 could be the reason for the very low PL efficiency ($< 1\%$) of PTCDA and similar compounds [47]. During the relaxation scenario discussed above, an inter-system crossing towards excited states without dipole-allowed transition to the ground state could take place. This would force the system to relax preferentially through non-radiative processes towards the electronic ground state.

9. – Heterostructures

Heterostructures of organic molecules have been grown in different material combinations, *e.g.* PTCDA/NTCDA and PTCBI/NTCDA [48], and PTCDA/indium-phthalocyanine-chloride (InPc-Cl) [49], where some of the absorption and PL results were interpreted on the basis of a theory for Wannier-Mott excitons [2, 50]. Models for Frenkel exciton transfer in ultrathin films have already been discussed before with phenomenological transfer parameters [51, 52]. These methods will now be applied together with the microscopic calculations of the interactions between the molecular transition dipoles discussed in sect. **6**.

The data for the PTCDA/InPc-Cl heterostructures are particularly suited for a generalization of the model approach developed in sect. **6** towards finite film thickness because they cover ultrathin films of 1 monolayer (ML) to 4 MLs PTCDA confined between spacer layers of 2 MLs of InPc-Cl [49]. As the absorption bands of PTCDA and

InPc-Cl are well separated, only a small region around 2.1 eV is difficult to assign to the contributions of the two materials.

As in sect. **6**, the model calculations discussed in the following will be based on the microscopic approach for the interaction of the spatially extended HOMO-LUMO transition dipoles [9, 41]. As the surrounding phthalocyanine layers have different transition energies and no well-defined geometric arrangement with respect to the PTCDA molecules, we can ignore any exciton transfer matrix element between the two materials. This introduces a strong change of the surroundings experienced by a PTCDA molecule in the final layer of the film, because the dominating matrix element for Frenkel exciton transfer to the stack neighbour, $W = 0.082$ eV, occurs only to the consecutive PTCDA layer. The Hamiltonian (10) discussed before has now to be extended in order to include basis molecules A and B within each monolayer, *i.e.* the basis size corresponds to the vibrational basis states $\nu = 0, ..., 4$ for the A and B molecules in each of the layers $n_z = 1, ..., N_z$. The Fourier transform of the Hamiltonian is now only possible within the plane corresponding to fig. 1, while the third component remains in the site representation with N_z layers. Concerning the interaction matrix elements, we perform again an integration over spheres with a radius of 35 unit cells, *i.e.* ellipsoids in real space, cf. sect. **6**. As the Fourier-transformed Hamiltonian is still formulated in the basis of the N_z layers, we have to compute the transfer matrix elements X and V of a reference molecule with an entire layer. Compared to eq. (13) and (14), this requires the generalization

$$X_{n_z m_z}(k_x = k_y = 0) = \sum_{j \neq 0}^{\text{layer } m_z} T_{0A;jA} \tag{21}$$

$$V_{n_z m_z}(k_x = k_y = 0) = \sum_{j}^{\text{layer } m_z} T_{0A;jB} \tag{22}$$

where the reference molecule belongs to layer n_z and the sums extend over the layer m_z. For the matrix elements X, it is again useful to distinguish between the interaction W with the stack neighbour, if present, and the remaining interactions M with the more distant molecules. The size of the matrix elements decreases again with distance: Up to the second neighbour plane, they are $M_{nn} = -0.014$ eV, $M_{n,n+1} = -0.009$ eV, and $M_{n,n+2} = 0.001$ eV for transfer to the same basis molecule in the other unit cells, and $V_{nn} = 0.013$ eV, $V_{n,n+1} = 0.006$ eV, and $V_{n,n+2} = 0.001$ eV for transfer to the other basis molecule, with all matrix elements to more distant planes below 1 meV. Therefore, inclucing the stack neighbour, the transfer matrix element $X_{n,n+1} = W + M_{n,n+1} = 0.073$ eV is by far the largest.

Concerning the reference energies E_{00}, we have to define reasonable estimates for the surface planes. For a single ML, we find a reference energy of $E_{00} = 2.33$ eV from a comparison with the experimental data [49], quite close to the value of 2.365 eV used for the dissolved monomers, cf. sect. **5**. As the two matrix elements $X_{nn} = M_{nn} = -0.014$ eV and $V_{nn} = 0.013$ eV and the resulting combinations $(X \pm V)$ are much smaller than the effective vibrational quantum $\hbar\omega = 0.17$ eV, the deformation of the

expected Poisson distribution over the different vibrational sublevels is small, and the lowest vibrational level dominates.

In fig. 12, we report the absorption coefficient resulting from $\epsilon_{||} = \frac{1}{2}(\epsilon_{xx} + \epsilon_{yy})$ calculated for different film thicknesses, with the same broadenings as in fig. 8. However, for the single ML, the experimental spectra reveal an increase of broadening compared to the dissolved monomers in fig. 7, although the higher harmonics remain still visible [49]. This is an indication that the broadening of the higher harmonics is not increased, cf. the discussion of fig. 8, which is reasonable for the 1 ML case because the parameters X_{nn} and V_{nn} are quite small. Therefore, it might be more realistic to compute the 1 ML spectra again, but with the same broadening of about FWHM $\approx \hbar\omega = 0.15$ eV for all the higher vibrational levels (not shown).

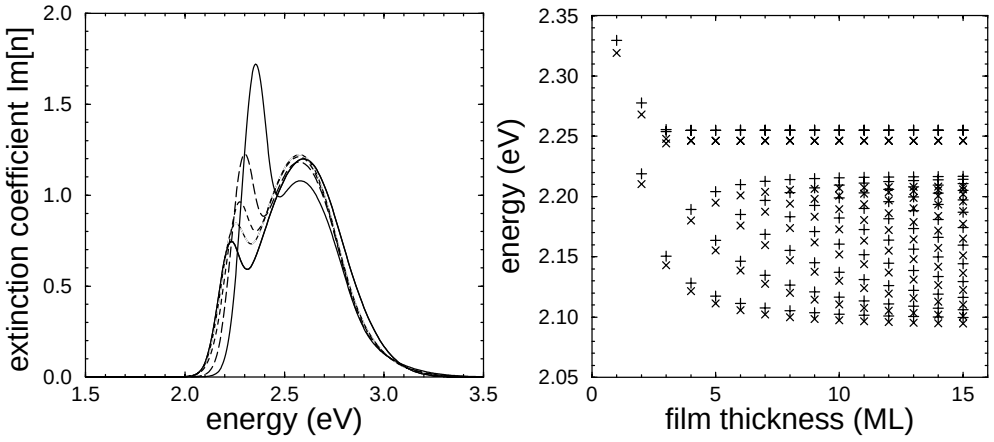

Fig. 12. – Left: comparison of the extinction coefficient $\Im[n]$ for $N_z = 1, 2, 4$, and 10 ML film thicknesses with the bulk reference. The reported curves are calculated with the broadenings of the different vibronic sublevels as in fig. 8. Solid line: $N_z = 1$, and bulk reference, cf. fig. 8. Long-dashed line: $N_z = 2$, short-dashed line: $N_z = 4$, dotted line: $N_z = 10$. Right: contributions to the lowest vibronic level, $\times$: lower Davydov component, contributing to ϵ_{xx}, $+$: upper Davydov component, contributing to ϵ_{yy}. The two uppermost states are localized at the two surfaces, while all others have envelopes resembling states in a quantum well with infinite barriers. For larger films, these energies are similar to a sampling of the dispersion $E_{00}(0, 0, k)$ in fig. 9 at equidistant wave vectors.

For the case of 2 MLs, each molecule has one PTCDA neighbouring plane, and one InPc-Cl plane. Therefore, we estimate E_{00} as the average between the single ML and the bulk value, $E_{00} = \frac{1}{2}(2.33 + 2.18)$ eV $= 2.255$ eV. For even larger films, we use the same surface energy, and the bulk value $E_{00} = 2.18$ eV for all inner planes. The dependence of the extinction coefficient on the layer thickness is reported in fig. 12. For increasing thickness, the influence of the higher reference energy E_{00} in the surface layers is reduced, so that the lowest vibronic transition converges to the bulk value. Concerning the high-energy edge around 2.8 eV, we observe that within the range of film

thicknesses investigated, the shift of the oscillator strength to the higher harmonics is not yet fully developed. This can be understood from the open boundary conditions: The interaction matrix elements X still have a smaller influence than in the bulk because the surface molecules are lacking one exciton transfer matrix element W. Furthermore, the miscroscopic calculation converges towards $V(\mathbf{0}) = 0.034$ eV, while the bulk reference has been computed with a somewhat higher value of $V(\mathbf{0}) = 0.047$ eV, fitted to the experimental spectra in fig. 8, cf. the discussion in sect. **6**.

Concerning each vibronic sublevel, the N_z different wavefunctions behave roughly as in a one-dimensional potential with infinite barriers, except for two surfaces states which are due to the changed on-site energy in the outermost layers. For the vibronic ground state, these surface states are the only ones above the bulk limit for the Davydov doublet, cf. fig. 12, while the highest pair of the remaining states converges to this limit. These states produce the highest oscillator strength, with envelopes resembling the lowest state in a quantum well with infinite barrier. In a **k**-space picture, this corresponds to the lowest possible wavenumber, or the best possible approach to the Γ point in the bulk. The present investigation demonstrates that surface states arise not only in models including both Frenkel and CT excitons [53]: In our model, they result from the energy shifts of the Frenkel excitons in the surface layers.

10. – Conclusion

In the present work, we have investigated the optical properties of PTCDA, both for dissolved monomers and crystalline films. Our calculations of the vibrational modes of a single molecule and the deformation in the relaxed excited state show good agreement with the observed absorption of dissolved molecules and resonant Raman spectra of thin films. The subsequent development of microscopic approaches for the transfer of Frenkel excitons between different molecules has allowed for a quantitative modelling of the observed linear optical properties of poly-crystalline PTCDA films. Furthermore, the corresponding **k**-space dispersion of the excitonic transitions, together with a detailed analysis of low-frequency internal vibrations and external phonon modes as observed in resonant Raman spectra, gives a hint for the origin of the very high Stokes shift observed between absorption and low-temperature PL spectra. A contribution to the PL spectra at lower energy can be interpreted on the basis of exciton dissociation and subsequent recombination between positively and negatively charged molecules. The required charge separation seems to involve a small barrier, so that the recombination between molecules in opposite charge states becomes dominant at higher temperatures. The application of the model of Frenkel exciton transfer to heterostructures with only a few monolayers revealed the existence of surface states, probably depending on the type of the surrounding material.

11. – Acknowledgement

We thank T. Fritz for the original data of Ref. [10], M. Hoffmann for the absorption spectra of the dissolved monomers, and H. Fröb, M. Garriga, and M. Knupfer for sharing unpublished data. Financial support by the EU funded Human Potential Research Training Network DIODE (Contract no: HPRN-CT-1999-00164) and by the Deutsche Forschungsgemeinschaft is gratefully acknowledged.

REFERENCES

[1] LOVINGER A. J., FORREST S. R., KAPLAN M. L., SCHMIDT P. H., and VENKATESAN T., *J. Appl. Phys.*, **55** (1984) 476.
[2] SO F. F. and FORREST S. R., *Phys. Rev. Lett.*, **20** (1991) 2649.
[3] BULOVIĆ V., BURROWS P. E., FORREST S. R., CRONIN J. A., and THOMPSON M. E., *Chem. Phys.*, **210** (1996) 1.
[4] FORREST S. R., *Chem. Rev.*, **97** (1997) 1793.
[5] SOOS Z. G., HENNESSY M. H., and WEN G., *Chem. Phys.*, **227** (1998) 19.
[6] HENNESSY M. H., SOOS Z. G., PASCAL R. A., and GIRLANDO A., *Chem. Phys.*, **245** (1999) 199.
[7] HOFFMANN M., SCHMIDT K., FRITZ T., HASCHE T., AGRANOVICH V. M., and LEO K., *Chem. Phys.*, **258** (2000) 73.
[8] SCHOLZ R., KOBITSKI A. YU., KAMPEN T. U., SCHREIBER M., ZAHN D. R. T., JUNGNICKEL G., ELSTNER M., STERNBERG M., and FRAUENHEIM T., *Phys. Rev. B*, **61** (2000) 13659.
[9] VRAGOVIĆ I., SCHOLZ R., and SCHREIBER M., *Europhys. Lett.*, **57** (2002) 288.
[10] DJURIŠIĆ A., FRITZ T., and LEO K., *Opt. Commun.*, **183** (2000) 123.
[11] SALVAN G., HIMCINSCHI C., KOBITSKI A. YU., FRIEDRICH M., WAGNER H. P., KAMPEN T. U., and ZAHN D. R. T., *Appl. Surf. Sci.*, **175-176** (2001) 363.
[12] KOBITSKI A. YU., SALVAN G., WAGNER H. P., and ZAHN D. R. T., *Appl. Surf. Sci.*, **179** (2001) 209.
[13] HOFFMANN M., and FRITZ T., private communication.
[14] GÓMEZ U., LEONHARDT M., PORT H., and WOLF H. C., *Chem. Phys. Lett.*, **268** (1997) 1.
[15] HERZBERG G., *Molecular Spectra and Molecular Structure, I. Spectra of Diatomic Molecules* (Krieger, Malabar) 1950, chapter IV.
[16] MAHAN G. D., *Many-Particle Physics* (Plenum, New York) 1981, chapter 4.3.
[17] LOUDON R., *The Quantum Theory of Light* (Clarendon, Oxford) 1983, chapter 2.4.
[18] MYERS A. B., and MATHIES R. A., in *Biological Applications of Raman Spectroscopy*, ed. by SPIRO T.G. (Wiley, New York) 1987, Vol. 2, p. 1.
[19] MARKEL F., FERRIS N. S., GOULD I. R., and MYERS A. B., *J. Am. Chem. Soc.*, **114** (1992) 6208.
[20] KAMPEN T. U., TENNE D. A., PARK S., SALVAN G., SCHOLZ R., and ZAHN D. R. T., *phys. stat. sol. (b)*, **215** (1999) 431.
[21] FRAUENHEIM T., SEIFERT G., ELSTNER M., HAJNAL Z., JUNGNICKEL G., POREZAG D., SUHAI S., and SCHOLZ R., *phys. stat. sol. (b)*, **217** (2000) 41.
[22] PERDEW J. P., BURKE K., and ERNZERHOF M., *Phys. Rev. Lett.*, **77** (1996) 3865.
[23] PEDERSON M. R., and LIN C. C., *Phys. Rev. B*, **35** (1987) 2273; POREZAG D. V., and PEDERSON M. R., *Phys. Rev. B*, **54** (1996) 7830.

[24] SCHOLZ R., KOBITSKI A. YU., KAMPEN T. U., SCHREIBER M., JUNGNICKEL G., and FRAUENHEIM T., *phys. stat. sol. (b)*, **221** (2000) 541.
[25] In our first assignment based on the density functional tight-binding method [8], we obtained a smaller r.m.s. deviation of 24 cm^{-1} for the A_g modes, but subsequent calculations based on the B3LYP functional [26] as implemented in the GAUSSIAN98 software package [27] resulted in some changes for modes with minor Raman cross sections. The latter method results in r.m.s. deviations of the A_g modes of 17 cm^{-1} [28].
[26] BECKE A. D., *Phys. Rev. A*, **38** (1988) 3098; LEE C., YANG W., and PARR R. G., *Phys. Rev. A*, **37** (1988) 785.
[27] FRISCH M. J., et. al., Gaussian98, Revision A.9, (Gaussian Inc., Pittsburgh PA) 1998.
[28] KOBITSKI A. YU., SCHOLZ R., and ZAHN D. R. T., *J. Molec. Struct. THEOCHEM*, (2001) submitted.
[29] KAMPEN T. U., SALVAN G., FRIEDRICH M., TENNE D. A., PARK S., and ZAHN D. R. T., *Appl. Surf. Sci.*, **166** (2000) 387.
[30] SALVAN G., TENNE D. A., DAS A., KAMPEN T. U., and ZAHN D. R. T., *Organic Electronics*, **1** (2000) 49.
[31] KAMPEN T. U., SALVAN G., TENNE D., SCHOLZ R., and ZAHN D. R. T., *Appl. Surf. Sci.*, **175-176** (2001) 326.
[32] UOSAKI Y., KITAURA S., and MORIYOSHI T., *J. Chem. Eng. Data*, **42** (1997) 580.
[33] FRÖB H., et al., unpublished.
[34] GUSTAV K., LEONHARDT M., and PORT H., *Monatshefte Chemie*, **128** (1997) 105.
[35] DAVYDOV A. S., *Theory of Molecular Excitons*, (Plenum, New York) 1971.
[36] AGRANOVICH V. M., and GALANIN M. D., *Electronic Excitation Energy Transfer in Condensed Matter*, (North-Holland, Amsterdam) 1982.
[37] ZANG D. Y., SO F. F., and FORREST S. R., *Appl. Phys. Lett.*, **59** (1991) 823.
[38] LANDAU L. D., and LIFSHITZ E. M., *Electrodynamics of Continuous Media*, 2nd edition (Pergamon, Oxford) 1984, §13.
[39] RESTA R., *Phys. Rev. B*, **16** (1977) 2717.
[40] ALONSO M. I., GARRIGA M., KARL N., OSSÓ J. O., and SCHREIBER F., *Organic Electronics*, **3** (2002) 23.
[41] VRAGOVIĆ I., SCHOLZ R., and SCHREIBER M., in preparation.
[42] KNUPFER M., et al., unpublished.
[43] HASCHE T., CANZLER T. W., SCHOLZ R., HOFFMANN M., SCHMIDT K., FRAUENHEIM T., and LEO K., *Phys. Rev. Lett.*, **86** (2001) 4060.
[44] KOBITSKI A. YU., SCHOLZ R., WAGNER H. P., and ZAHN D. R. T., *Phys. Rev. B*, (2002) submitted.
[45] NOWAKOWSKA M., SMOLUCH M., and PETELENZ P., *Chem. Phys. Lett.*, **270** (1997) 234.
[46] NISHIMURA H., YAMAOKA T., MIZUNO K., IEMURA M., and MATSUI A., *J. Phys. Soc. Jpn.*, **53** (1984) 3999.
[47] NOLLAU A., HOFFMANN M., FLORECK K., FRITZ T., and LEO K., *J. Appl. Phys.*, **87** (2000) 7802.
[48] HASKAL E., SHEN Z., BURROWS P. E., and FORREST S. R., *Phys. Rev. B*, **51** (1995) 4449.
[49] ANDERSON M. L., WILLIAMS V. S., SCHUERLEIN T. J., COLLINS G. E., ENGLAND C. D., CHAU L.-K., LEE P. A., NEBESNY K. W., and ARMSTRONG N. R., *Surf. Sci.*, **307-309** (1994) 551.
[50] SHEN Z., and FORREST S. R., *Phys. Rev. B*, **55** (1997) 10578.
[51] SAJFERT V., TOŠIĆ B. S., MARINKOVIĆ M. M., KOZMIDIS-LUBURIĆ, *Physica A*, **166** (1990) 430.

[52] ŠETRAJČIĆ J. P., STOJKOVIĆ S. M., LAZAREV S. B., VRAGOVIĆ I. D., MIRJANIĆ D. LJ., *SPIE-PL Proc. 5th Conf. Dielectric and Related Phenomena*, **37DP** (1998) 162.
[53] AGRANOVICH V.M., SCHMIDT K., LEO K., *Chem. Phys. Lett.*, **325** (2000) 308.

contribution for proceedings of
SCUOLA INTERNAZIONALE DI FISICA "ENRICO FERMI", course CXLIX
Organic Nanostructures: Science and Applications
(revised version: 20 December 2001)
(final corrections: 04 June 2002, according to proofs received 29 May 2002)